Automated targeted sectioning of resin-embedded hard tissue specimen using micro-computed tomography in combination with laser microtomy

P. Nolte and C. J. Gröger, C. Frey, H. Richter, F. Will, T. Bäuerle, A. F. Schilling, F. Alves, C. Rußmann and C. Dullin

***Abstract*— *Objective*: Histological analysis of hard tissue specimens is widely used in clinical practice and preclinical research, but it remains a labor-intensive and destructive process. In particular, resin-embedded tissues present challenges due to the inability to target regions of interest (ROI), as internal structures are not visible externally. This work proposes a guided sectioning workflow that enables precise targeting of concealed ROIs using a multimodal approach. *Methods*: By combining microCT imaging with an automated cutting system, and laser microtomy, precise *targeted sectioning* was achieved. MicroCT imaging enables visualization of internal structures, guiding the automated cutting system for precise sectioning. Laser microtomy then allows thin tissue sections to be prepared while preserving diagnostic features. *Result*: Comparing the automated workflow to the conventional cutting-grinding technique showed that the new method improved accuracy by a factor of 7 and reduced material loss by half and processing time by 75%. Validation was performed by comparing the histological sections with *in silico* target planes generated from the microCT scans, showing precise alignment between the targeted regions and the prepared sections. *Conclusion:* We demonstrate that the proposed approach significantly reduces tissue loss and offers a more efficient workflow compared to traditional methods. Additionally, microCT-based targeting enables accurate correlation between histological findings and 3D pathological structures. *Significance*: The automated guided sectioning workflow provides valuable insights into tissue pathology, enhancing clinical diagnostics and preclinical research. It also facilitates the generation of multimodal datasets, which can be used in future machine learning applications.**

***Index Terms*— Computed Tomography, Hard Tissue, Histology, Image Registration, Sectioning, Image Processing, Digital Pathology, Multimodal Fusion, Correlative Imaging**

The authors acknowledge the support of the German Federal Ministry of Education and Research (BMBF) [grant number CT_LASER_BONE 13FH215PX8]. The funding institutions had no role in the study design, collection, analysis, and interpretation of the data, in the writing of the manuscript, and in the decision to submit the manuscript for publication. Parts of the present work are subject of a patent application. Authors Heiko Richter and Fabian Will are employees of LLS ROWIAK LaserLabsSolutions GmbH, a company that may have a potential interest in commercializing aspects of this work.

P. Nolte and C. J. Gröger contributed equally to this work. Equal supervision by C. Russmann and C. Dullin. Corresponding authors: C. Rußmann and C. Dullin

P. Nolte, C. J. Gröger, C. Frey are with the Faculty of Engineering and Health, University of Applied Sciences and Arts Göttingen, Von-Ossietzky-Straße 99, 37085 Göttingen, Germany (E-mail: philipp.nolte1@hawk.de, chris.groeger1@hawk.de, christopher.frey@hawk.de)

H. Richter and F. Will are with the LLS Rowiak LaserLabSolutions GmbH, Garbsener Landstraße 10, 30419 Hannover, Germany (E-mail: h.richter@lls-rowiak.de, f.will@lls-rowiak.de)

T. Bäuerle was with the Department of Radiology, University Hospital Erlangen, Ulmenweg 18, 91054 Erlangen, Germany) and is now with the Department of Diagnostic and Interventional Radiology, University Medical Center of Johannes-Gutenberg-University, Langenbeckstraße 1, 55131, Mainz, Germany (E-mail:tobias.baeuerle@uk-erlangen.de)

A. F. Schilling is with the Department of Trauma Surgery, Orthopedics and Plastic Surgery, University Medical Center Göttingen, Robert-Koch-Straße 40, 37085 Göttingen, Germany (E-mail: arndt.schilling@med.uni-goettingen.de)

F. Alves is with the Translational Molecular Imaging Group, Max Planck Institute for Multidisciplinary Sciences, Hermann-Rein-Straße 3, 37085 Göttingen, Germany University Medical Center Göttingen, Institute for Diagnostic and Interventional Radiology and Department of Haematology and Medical Oncology, Robert-Koch-Straße 40, 37085 Göttingen, Germany (E-mail: falves@gwdg.de)

C. Rußmann is with the Faculty of Engineering and Health, University of Applied Sciences and Arts Göttingen, Von-Ossietzky-Straße 99, 37085 Göttingen, Germany, and Brigham and Women's Hospital, Harvard Medical School, 75 Francis S, Boston, ME 02115, USA (E-mail: christoph.russmann@hawk.de)

C. Dullin is with the Translational Molecular Imaging Group, Max Planck Institute for Multidisciplinary Sciences, Hermann-Rein-Straße 3, 37085 Göttingen, Germany University Medical Center Göttingen, Institute for Diagnostic and Interventional Radiology,Robert-Koch-Straße 40, 37085 Göttingen, Germany and Department for Diagnostic and Interventional Radiology, Im Neuenheimer Feld 400, 69120 Heidelberg, Germany (Email: christian.dullin@med.uni-goettingen.de)

I. Introduction

PATHOLOGICAL changes in biological tissue can often only reliably be analyzed on a cellular level. Therefore, histology - the microscopic analysis of stained micrometer thin tissue sections - is a widely used method in clinical routine as well as in biomedical research. Since histology requires cutting, which destroys the specimen in the process, it is of utmost importance to utilize this approach to its full potential. In most cases, formalin-fixed and paraffin-embedded (FFPE) tissue is used and cut with a static blade. However, this approach does not work for undecalcified bone specimens. Especially in research of bone diseases like osteoporosis, bone cancer, or bone metastasis, local changes in

the mineral concentration of the bone are important hallmarks of bone lesions and should therefore not be removed in a decalcification process. Typically, undecalcified specimens are embedded in resin and processed by the so-called cutting-grinding approach [1] also resulting in thin sections, but only in combination with substantial material loss.

Histological sectioning is typically performed without precise targeting because embedding materials are often partially opaque or distort the tissue. For instance, in FFPE specimens, the paraffin encases the tissue, and regions of interest are usually located within the specimen, making it difficult to accurately target specific structures. Although the resin used for embedding is usually transparent, it distorts tissue perception, complicating the manual definition of a precise cutting plane based solely on visual inspection. As a result, there is a significant risk of missing or damaging critical tissue structures, which can lead to diagnostic errors or necessitate further invasive procedures, such as additional biopsies.

As a supplement to the classical histology routine, 3D imaging techniques such as microCT have been proposed [2]. Through this extension, researchers have been exploring the advantages of multimodal correlation of microCT 3D scans and 2D histological sections as presented for example by Albers et al. [3]. Here a microCT scan of the uncut block was employed to i) identify structures of interest and ii) use the post-cut information for image fusion of both modalities. However, a significant drawback of this approach is the limited ability, to plan the sectioning procedure, as there is no geometrical reference between the microCT data set and the cutting device. Thus, cutting planes are typically marked on the surface of the resin block by hand based on reference structures visible in both the obtained CT scans and the physical appearance of the specimen. This technique is inherently prone to error and cannot guarantee a precise realization of the desired cutting position. Moreover, the method does not allow a high throughput as the manual marking of a cutting plane based on the microCT data is very time-consuming. Current research indicates the demand for the implementation of an automated cutting system. For example, Meechan et al. [4] presented an automated ultramicrotome-based sectioning method to extract desired cutting planes from resin-embedded specimens to perform electron microscopy. Their approach, however, still requires manual steps such as the alignment of the blade to the top of the resin block, which was used as a geometrical reference to align both microCT data and the cutting system. Typically, only small resin blocks that contain undecalcified hard tissue with a surface area of about 1.5 mm x 1.5 mm, as reported by Hua et al. [5], are compatible with ultramicrotome sectioning. For decalcified specimen the surface area can be larger. Thus, the size of tissue samples that can be processed is restricted.

MicroCT systems are widely used tools in biomedical research [6]. While the contrast of classical microCT for soft tissue is typically limited and needs to be boosted by additional staining procedures as reported by Metscher et al. [7], the scanning of hard tissue specimens at resolutions down to a few micrometers can easily be achieved. Scanning times strongly depend on the desired spatial resolution and image quality. In the case of standard bench-top microCT, it ranges roughly from minutes to hours. The technical improvement in this perspective suggests that microCT will become an interesting tool to also analyze bone specimens in clinical routine in the near future [8].

Our method not only allows to precisely target a region of interest (ROI) but is also characterized by substantially lower material loss and the ability to perform nearly serial sectioning. This is achieved by the incorporation of microCT data before and after sectioning in combination with a computer-controlled positioning system and laser microtomy [9], [10]. Laser microtomy, is a contact-free sectioning methodology that generates thin sections (between 10 and 50 µm) by traversing femtosecond laser pulses through a resin block with no deformations, which is a significant advantage compared to microtome sectioning of decalcified hard tissue. The laser is focused inside the tissue at a defined depth by a high numerical aperture (NA) objective lens ($NA > 0.5$) resulting in a lateral spot size of approximately 1-2 µm (estimated value, not measured). Photodisruption occurs in the focal volume which sublimates the material [9]. The exact value of the removed material by the laser cutting process is unknown but the loss of material between two consecutive laser microtomy sections is approximately 20-30 µm (unpublished data of LLS ROWIAK) including final grinding of the residual tissue block after separation of the section. A histological slice is generated by raster scanning the laser over the entire cross-section of the embedded specimen. However, due to the limited penetration depth of the laser, still a priming cut with a conventional pathological saw is required.

Here we present an automatic approach for guided sectioning in hard tissue histology. Since our method significantly improves the accuracy, reduces the time spent, and minimizes the material loss in comparison to the classical cutting-grinding approach, it has great potential for use in for instance applications of digital pathology, where precise multimodal investigation of tissue specimens is essential.

II. Methods

A. Specimen preparation and embedding protocol

All specimens were embedded in a 25 mm or 40 mm wide embedding mold using either a methacrylate (MMA) based agent (Technovit 9100, Kulzer) resin or standard commercially available epoxy resin (UNIVERSAL E45, BBI-Trade GmbH). If necessary, the polymerized blocks were extended by gluing them on spare resin blocks to ensure that the ROI was positioned outside of the cassette. For induction of bone metastasis nude rats (RNU Strain, Charles River, Germany) were injected with human MDA-MB-231 breast cancer cells in the right superficial epigastric artery in order to facilitate tumor growth in the hind limb, as previously described by Bäuerle et al. [20]. Animals developed osteolytic bone metastases at the hind

limb including the femur and tibia around the knee joint. Upon sacrifice, the right hind legs were removed and prepared for fixation with 70% ethanol and embedded in Technovit 9100 NEW (Kulzer, Hanau, Germany).

B. MicroCT acquisition

After hardening, the blocks were scanned in an *in-vivo* microCT (Perkin Elmer, Quantum FX) using the following settings: tube voltage 90 kV, tube current 200 µA, field of view 60x60 mm^2 and a total acquisition time of 15 min resulting in an isotropic resolution of 118 µm. An inherent filtration of 100 µm of aluminum (Al) and 60 µm of copper (Cu) is used to suppress beam hardening artifacts [21]. Each resulting data set yielded a dimension of 512x512x512 voxels and a 16-bit gray value range. Two consecutive scans were performed and stitched together to cover both the specimens and the cassette. All scans were saved in the Vox1999a-Format (.vox). The specimens were scanned using a proprietary holder that ensured reproducible positioning. Renderings were generated using Scry (developed by C. Dullin) and VG Studio V. 3.2.1 (Volume Graphics GmbH).

C. Sectioning process and microscopy

For our novel workflow, we remodeled a pathological saw (cut-grinder primus, Walter Messner GmbH). After the cut, the specimens were glued to a glass slide (X-tra-Adhesive, Leica Biosystems) and then sectioned using a laser microtome (Tissue Surgeon, LLS Rowiak LaserLabSolutions GmbH). The use of laser microtomy allowed the generation of about 10 to 15 µm thick consecutive slides. Here, after sectioning the block is again polished, glued to a new glass slide, and cut again. This process is repeated until no material is left. For the specimen processed with the classical cutting-grinding technique, the priming cut was performed using a different saw (Exakt 300, EXAKT Advanced Technologies GmbH). The sections were prepared using a grinding machine (EXAKT 400CS, EXAKT Advanced Technologies GmbH) resulting in a thickness of less than 10 µm. Here standard glass slides were used. All tissue specimens were stained using a modified Sanderson Rapid Bone Stain [16] and counterstained with van Gieson [17].

D. Software development

All software components concerning the functional realization of the proposed workflow were implemented in C++ and compiled using Visual Studio 15 2017. The 3D rendering of the microCT scans used for the definition of the *in silico* cutting plane was performed using VTK 8.2 [22]. 2D image processing was implemented based on OpenCV2 [23]. The user interface was designed using QT 5.14.2 [24].

The results were evaluated using a Python 3.8.8 script based on relevant packages like NumPy 1.23.1 [25], scikit-learn 1.2.0 [26], scikit-image [27] and OpenCV 4.6.0.66 [23]. Registration was performed using SimpleITK 2.2.1 library [28]. Development and usage have been realized through Python-based Jupyter 4.11.1 notebook [29]. 3D visualization used for coarse and quick verification inside the jupyter notebook was implemented using the Mayavi library 4.7.4 [30].

E. Creation and procession of the phantoms

All cone-shaped reference structures and the femurs models containing screws were created using casting powder (Raysin 200, Rayher Hobby GmbH) and custom-made silicone molds. The phantoms were embedded in standard commercial epoxy resin and cut using a standard pathological saw (Exakt 300, EXAKT Advanced Technologies GmbH) and the improved saw (see section 5.3, cut-grinder primus, Walter Messner GmbH). For the phantoms mimicking femurs, M2 plastic screws were used (Linsenschrauben, Bäcker GmbH & Co. KG - Kunststoff - Metall - Normelemente). Distance measurements necessary to draw the manual cutting plane on the resin blocks were performed using the software Scry.

F. Hardware development

The positioning system was constructed using two rotational stages (DMT 65, OWIS GmbH) and one linear stage (LTM 120, OWIS GmbH). The software/hardware interface was implemented using a 3-axes-control system unit (PS 35, OWIS, GmbH).

III. Results

The multimodal workflow for the automated *targeted sectioning* in hard tissue specimens demonstrates the benefit of our approach in comparison to classical cutting-grinding. In addition, the validity of our results was evaluated using similarity metrics and geometrical offsets, a methodology we have already established in our previous work [11], [12].

A. General structure

The presented workflow has been devised as an extension to the standard protocol for histological analysis of non-decalcified hard tissue specimens. To assess the efficacy of our method, we compared exemplary cuts and subsequent outcomes of the novel workflow with those obtained through the traditional cutting-grinding technique, employing specific 3D phantoms. We used these phantoms for the purposes of correlating microCT and histology as well as to ease the comparison of the two sectioning workflows, as previously explored in our prior research [12]. Commencing with a microCT scan of the specimen (Figure 1A), a user-defined cutting plane was established, based on the visual examination of the scan (Figure 1B). The desired *in silico* planned cutting plane was then realized by a motorized positioning system, placing the specimen in front of the saw at the correct location and in the correct orientation (Figure 1C). The now-revealed intrinsic ROI was further processed by laser microtomy (Figure 1D and E). The material loss can be estimated based on the width of the saw band (about 0.7 mm) and the sectioning thickness of typically 30 to 40 µm. After additional fine grinding (resulting in sections with a thickness of about 10 to 15 µm) (Figure 1F),

the sections were stained, imaged (Figure1G), and compared with the *in silico* plane in the microCT data set to validate the efficacy of the described methodology. The workflow is depicted in Figure 1.

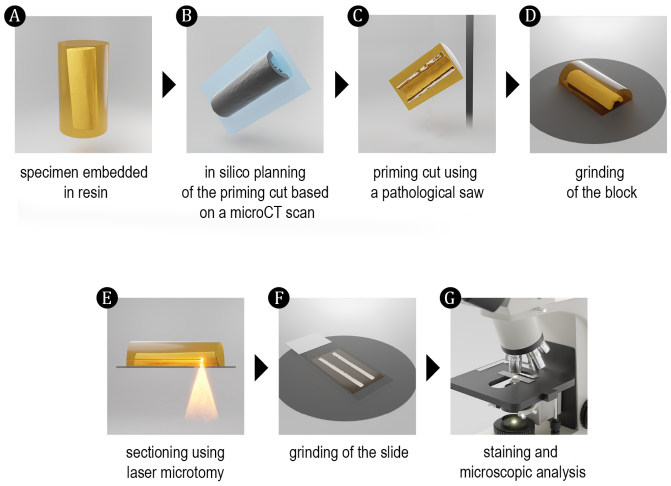

Fig. 1. Visualization of single steps realized in the implemented workflow. After the specimen is embedded in resin (A) an ROI is identified in a microCT scan inside of a hard tissue specimen. Based on the ROI an *in silico* cutting plane is determined by an expert (B). In order to realize the *in silico* cutting plane the tissue sample is autonomously positioned in front of the saw and subsequently cut (C). The exposed ROI is then finely ground (D) and sectioned using laser microtomy (E). All resulting sections require additional grinding (F) and are finally stained for microscopy (G). Following the digitization of each slide, the offset between the *in silico* cutting plane and the histological image is calculated, and the positioning parameters are optimized accordingly.

B. Design of the cutting system

The implemented cutting system extended the capabilities of the commercial pathological saw (cut-grinder primus, Walter Messner GmbH). For this, the device required several modifications. First, the saw was modified in order to fit into a new frame and the water cooling system was optimized using custom 3D printed parts resulting in a controlled laminar flow around the saw (Figure 2B). Second, the positioning process was automated by re-engineering the specimen holder and combining it with three computer-controlled actuators as visualized in Figure 2A. To ensure optimal performance, the aluminum profile-based frame was mounted on adjustable feet. Moreover, a metal plate was affixed to the top of the frame, which served as an interface between the positioning system and the saw. The foundation of the positioning system was a sled, which allowed a controlled movement towards the band. A linear stage was employed to enable precise longitudinal displacement of the specimen, orthogonal to the cutting direction. Additionally, two rotation angles, one around the central axis of the cassette and one tilting the specimen holder towards the saw, were realized utilizing two interconnected rotational stages. A Computer-aided design (CAD) simulation of the described system is shown in Figure 2A. All specimens utilized were carefully positioned within a distinctive proprietary cassette. The cassette plays a key role in the entire process as it allows linking the coordinate system of the microCT data with the coordinate system of the positioning system. The cassette was securely fastened into place by employing a specialized cassette holder. Considering the critical importance of cooling and cleaning the saw during the cutting process, the mentioned water protection equipment was specifically designed to fulfill this requirement. (see Figure 2B). To mitigate potential localized deviations in the cutting plane, a wheel-based guiding mechanism was implemented to stabilize the saw band (see Figure 2B). This effectively reduced variations in the saw band position during the cutting process, thus ensuring consistent and accurate results.

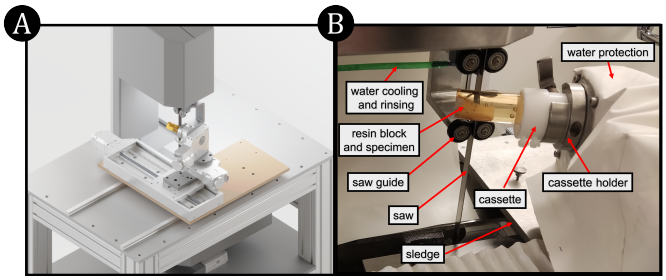

Fig. 2. Design of the priming cutting machine for resin-embedded hard tissue specimen. The commercially available pathological saw was placed inside a dedicated frame to ensure rigid fixation (A). Below the defined cutting position, a metal plate serves as the foundation for the pulley-based sled, which moves the positioning system toward the blade. On top of the sled the positioning system, composed of a linear stage, two rotational stages, and the cassette holder, was mounted. A close-up photograph of the positioning system is depicted in (B). The cassette and subsequent specimen are clamped into the cassette holder, thus attaching it to the positioning system. The sled is moved forward in order to position the specimen in front of the saw. A wheel-based saw guide was installed to mitigate the vibrations of the band saw system. Cooling and cleaning were paramount to the functionality of the separation process, which prompted the creation of a water protection cover for the positioning system.

C. Design of the specimen cassette

The cassette is subdivided into a three-point clamping arrangement, with an upper clamping mechanism consisting of two planes and a screw to secure the specimen. Below the fixed specimen, a reference structure was designed which is comprised of three orthogonal planes, facilitating precise reproducible mounting of the cassette. An exemplary rendering of the cassette is shown in Figure 3. The normal vector of the inferior plane (blue) defines the z-axis of the reference coordinate system, while the normal vectors of the left (red) and right (green) plane define the x and y axis respectively. The origin of the coordinate system is established at the *in silico* intersection point of all three planes. During the pre-cutting process, the cassette is firmly secured within the cassette holder (see Figure 3A), where it is clamped under the influence of an eccentric lever. Thus, the holder ensures sufficient force distribution across all planes and allows the reproducible positioning of the specimen cassette (see Figure 3B).

D. Detection of the reference coordinate system

The digital twin volume, of the specimen, reconstructed from the microCT scan, was loaded into our software and

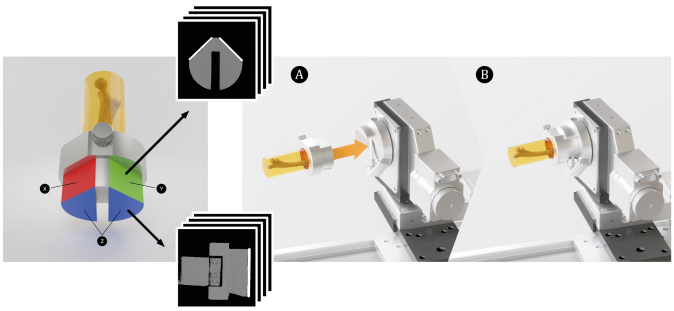

Fig. 3. Design of the specimen cassette and its complementary counterpart in the positioning system. The cassette serves as a secure enclosure for a hard tissue sample embedded in a resin block, enabling precise addressing of a specific *in silico* cutting plane (left). The cutting plane is defined in relation to three reference planes, represented by the colors red, green, and blue, corresponding to the axes x, y, and z respectively. After the microCT scan is completed and the reference planes are detected, the cassette is placed in a designated holder (A) and connected to the positioning system. By aligning the reference coordinate origin derived from the reference planes with the corresponding geometric point on the positioning system (B), the desired *in silico* cutting plane is accurately realized.

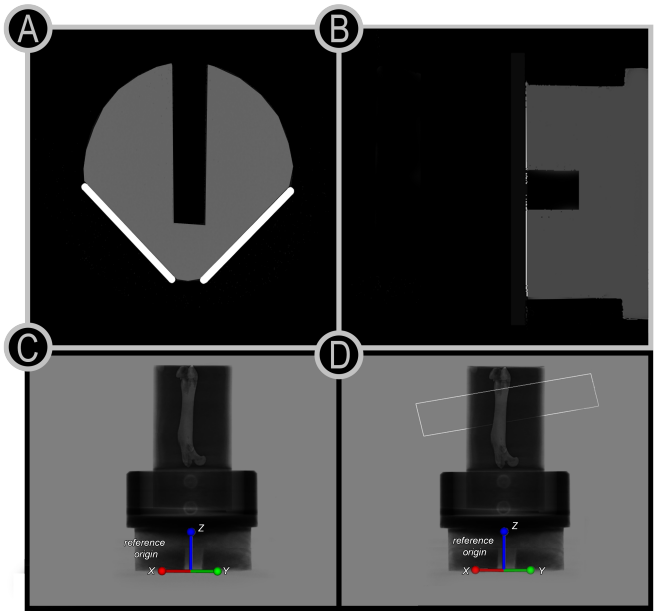

Fig. 4. Detection of the reference planes and subsequent computations of the reference origin and the coordinate system. The lateral reference planes are detected using a Hough Line detection algorithm, in the xy-planes (A). A custom version of a ray tracing algorithm is used to sample the inferior plane (B). Following the computation of the coordinate system, a reference gizmo (C) is placed into the volume to visually guide the user. Finally, a user-defined *in silico* cutting plane is inserted (D).

subsequently rendered. To establish an equivalent coordinate system within the *in silico* representation of the specimen, we detected the reference planes of the cassette as described above, allowing the definition of an analog coordinate system on the positioning device and in the *in silico* volume. The identification of the reference planes was accomplished by applying a Hough Line detection algorithm [13] (Figure 4A), coupled with a custom ray tracing algorithm (Figure 4B). The outcome of this process was the acquisition of individual data points and their respective 3D positions, resulting in the creation of three distinct point clouds, each corresponding to one of the reference planes. Subsequently, a principal component transformation [14] was conducted on each of these point clouds, which resulted in the calculation of the normal vectors of the respective planes. The line of intersection between the two lateral planes was computed and extended to pierce the inferior plane. Finally, the origin of the reference coordinate system was calculated as the point of intersection between this extended intersection line and the inferior reference plane. The basis vectors for the coordinate system were computed through the cross-product of the plane normal vectors of the lateral reference planes (Figure 4C). Following the detection of the coordinate system, the user can define a cutting plane (Figure 4D). Figure 4 visualizes the detection of the reference planes and the subsequent calculation of the new coordinate system.

E. Manual definition of the in silico cutting plane

After the identification of the reference coordinate system within the *in silico* microCT volume, the software allows the precise positioning of a user-defined cutting plane. Through rotational and translational adjustments until a desired ROI is found, the user is able to manipulate the position of the plane according to specified values along a designated axis. The cutting plane definition allows for manipulation in six degrees of freedom, thus granting the user extensive customization and control. During the positioning of the cutting plane a separate window is shown, visualizing the current sliced *in silico* volume. This image is saved for each performed cut, allowing for the multimodal fusion with the histological data.

F. Computation of the cutting parameters

The described workflow mapped the *in silico* microCT volume to its analog twin mounted in the positioning system. Using the geometrical information of the user-defined plane, the ROI is isolated automatically. First, the machine's native coordinate system was transformed to match the reference coordinate system, which in turn represented a defined structure on the physical cassette. After the transformation of the plane normal vectors into the coordinates of the reference system, the two rotational angle offsets (rot_1 and rot_2) were computed. These angles are depicted in Figure 5. The specimen is first tilted towards the saw, by calculating the angle rot_1 between the *in silico* cut plane normal vector z-component and the z-axis of the reference coordinate system. Thus, the calculation of the rot_1 simplifies to:

$$rot_1 = cos^{-1}|n_z| \tag{1}$$

rot_2 is the angle at which the cassette needs to be rotated around its z-axis. By projecting the normal vector into the xy-plane n_{xy}, rot_2 (the angle towards the y-axis) is computed as:

$$rot_2 = \frac{n_x}{|n_x|} * cos^{-1}\frac{-n_y}{\sqrt{n_x^2 + n_y^2}} \tag{2}$$

Since the longitudinal offset Y, realized with the before mentioned linear stage, is directly dependent on the tilt expressed

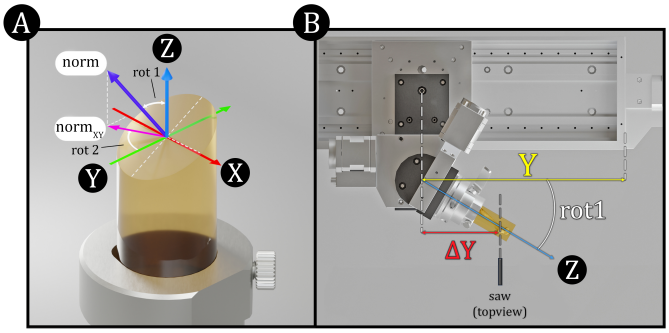

Fig. 5. Explanatory renderings depicting the significant factors for the calculation of the rotational and translational offsets. Following the detection of the reference coordinate system, and the definition of a cutting plane, the two adjustable angles $\boldsymbol{rot_1}$ and $\boldsymbol{rot_2}$ are computed (A). For $\boldsymbol{rot_1}$ the angle between the 3D normal vector of the cutting plane and the z axis is determined. $\boldsymbol{rot_2}$ yields the angle between the projected normal vector into the xy-plane (2D) and the y-axis. Following the calculation of the rotational offsets, the travel of the linear stage $\boldsymbol{Y}$ is derived (B). Based on $\boldsymbol{rot_1}$ the linear travel is shortened by $\boldsymbol{\Delta Y}$, thus demanding an additional subtraction from the full translational offset $\boldsymbol{Y}$.

in rot_1, one may simplify the calculation to a geometrical problem and solve for the hypotenuse $hypo$ of the triangle depicted in Figure 5B formed by the distance between the saw and the origin of the linear axis Y_{saw}:

$$Y = Y_{saw} + cos(rot_1) * hypo \tag{3}$$

G. Comparison of the classical cutting-grinding technique with the novel guided sectioning approach

We derived the positions of the saw and the positioning system from an ideal CAD simulation, which however did not completely reflect the actual structure. In order to compensate for possible offsets, we used acrylic glass cylinders, which were cut at predefined different positions and angles. The realized cutting planes were obtained from a subsequently performed second microCT scan. The translation and rotations of the *in silico* planed plane and the realized cutting plane were compared. Based on the average mismatch in these parameters the system was calibrated.

Following the calibration of our system, we compared the performance of our automated approach to the classical cutting-grinding technique. To this end, two groups of phantoms were used. In the first group, we embedded three cone-shaped reference structures that were connected using a disc at the base. This represents an extension of our previous work described in [12]. Each cone is identifiable in both the microCT scan and the histological section. By comparing the diameter of the sectioned cone, which appears as an ellipse in the 2D image, the height at which the sample was sliced can be determined. This process is repeated for all three cones, allowing the cutting plane to be accurately computed. The found *in silico* plane is then extracted from the volume and rigidly registered with the histological section. In the second group, phantoms mimicking femoral bones were used, where in each a plastic screw was placed manually. These represent a common use case in the analysis of calcified tissue containing extrinsic structures as shown for example in [15]. For the cone-based phantoms we manually defined cutting planes at certain heights and angles to perform these cuts as precisely as possible not only by an experienced technician, but also with our new cutting system. We measured the distances between the planned plane to the visible markings using the CT rendering software Scry and marked the ideal cutting plane on the resin blocks by hand. The screws in the second group of phantoms were interpreted as an important ROI aiming to visualize the center plane of each screw. Here, the technician was tasked to isolate the screw once without any additional information. This represented a challenge since the only visual reference to the screw's location is the head on the outside of the phantoms, which in turn is embedded in resin. In order to show the advantages of not only intrinsic microCT imaging but also an automated cutting system, the technician was also tasked to section another set of femur-like phantoms, on which an ideal cutting plane was marked on the block. While for this group of phantoms, the targeting of the ideal cutting plane was severely simplified, the sectioning process was still characterized by the cumbersome manual alignment of the block in front of the saw and the grinding of the specimen. Both the cone-shaped reference structures and femur-like phantoms are depicted in Figure 6. In order

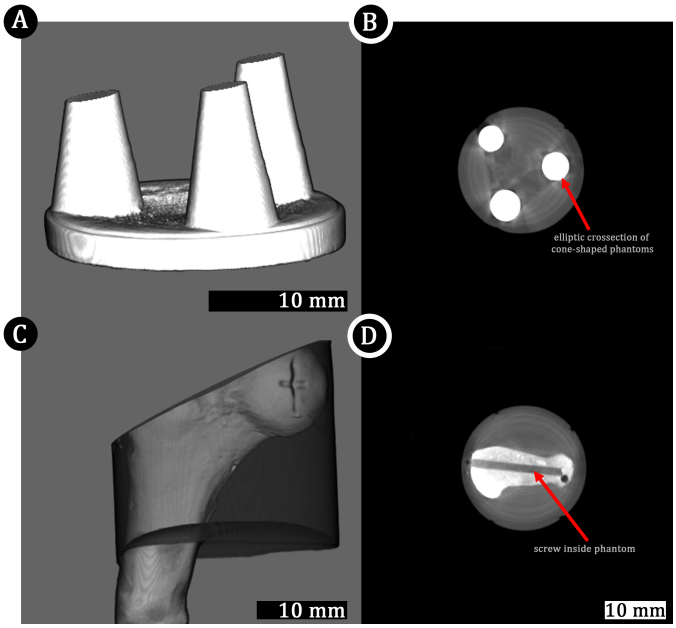

Fig. 6. MicroCT scans of the phantoms used for the exemplary cuts. (A) shows a newly developed cone-shaped reference structure, while the desired cutting plane depicting the resulting conic sections is shown in (B). Samples of the second group of phantoms mimicking femurs were also embedded in resin (C). The goal for using these sections was the extraction of the central plane for the inserted screw as shown in (D). These femur-like phantoms were processed with and without additional guidance based on markings on the resin block.

to quantify the quality of our approach we compared the manual and automated cuts of the cone-shaped reference structures based on three figures of merit: i) the time required to scan, cut, and prepare the slide, ii) the average amount of material used to generate one slide, and iii) the achieved positional offsets. For the manual cutting-grinding techniques

the six specimens were scanned and marked as described above. Samples given to a trained technician were manually positioned, cut, ground, and glued to slides, cut again, and finally ground. For our novel workflow each specimen was scanned in a cassette, and the developed software was used to i) plan the cutting plane and ii) automatically position the specimen in front of the saw. Following the priming cut, we sectioned the block using laser microtomy. After the completion of both workflows, one slide from each phantom was sectioned. For each workflow, we defined three types of cutting planes: straight, tilted at one angle, and titled at two angles. We processed two phantoms for each type of cutting plane, resulting in six phantoms cut by our technician and another six used for our *targeted sectioning* approach. Positional offsets were determined by computing the distance of both planes at the central axis of the system. Material loss was determined by weighing the specimens before and after sectioning. The results of our six conic specimens for each group can be found in Table I and show that the novel workflow was on average almost 4 times faster and needed about half of the specimen material to generate a histological slice of approximately the same thickness achieved with the classical method. In addition, the novel approach showed an average positional mismatch from the predefined *in silico* plane to the performed cut of about 0.15 mm, while the classical workflow only achieved an accuracy of about 1 mm. The phantoms containing the plastic screws were processed in three groups: i.) without any markings and the technician was asked to estimate where the screw was placed inside the specimen (see Figure 7 without guidance manually performed) ii.) the ideal cutting plane was defined using a microCT scan of the specimen and marked on the outside of the resin block (see Figure 7 with guidance manually performed) and iii) the specimens were processed using the automated workflow (see Figure 7 novel automated workflow). A qualitative overview of the achieved results is presented in Figure 7. Without prior knowledge of the position of the screw, achieving accurate sectioning is a significant challenge. To tackle this issue, we employed a dedicated definition of the cutting plane step and automated positioning, effectively minimizing potential offsets. While microCT-based planning vastly improves manual sectioning, it is still prone to random errors. In contrast, automated alignment of the specimen in front of the saw resulted in robust and accurate isolation of the ROI.

TABLE I

PERFORMANCES ACHIEVED BY THE MANUAL IN COMPARISON TO THE NOVEL AUTOMATED WORKFLOW. ALL RESULTS CONCERNING THE TIME, MATERIAL, AND POSITIONING OFFSET MEASUREMENTS USING THE SIX CONE-SHAPED REFERENCE STRUCTURES FROM EACH CUTTING PLANE GROUP WERE AVERAGED.

workflow	average time required per phantom [min]	average material processed per phantom [%]	mean positioning offset [mm]
manual cutting-grinding technique	278.07 ± 1.55	6.35 ± 2.32	1.04 ± 0.44
novel guided sectioning workflow	69.71 ± 2.59	3.36 ± 1.69	0.15 ± 0.12

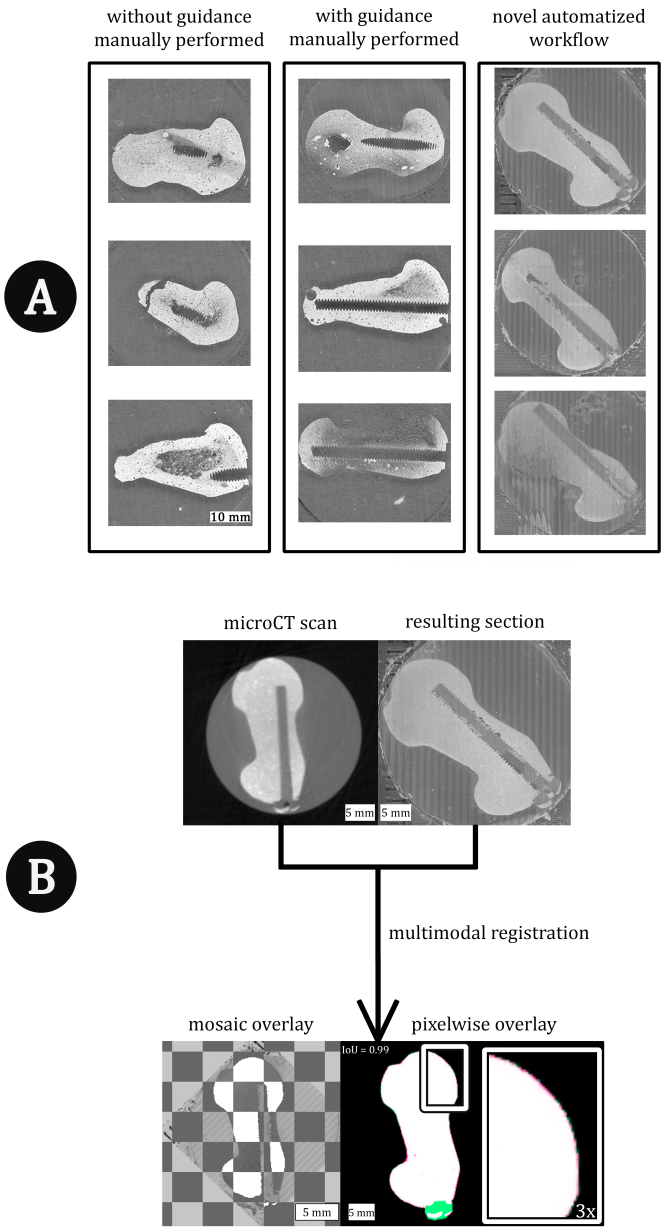

Fig. 7. Qualitative (A) and quantitative comparison (B) of the manual cutting-grinding technique and our novel guided sectioning workflow. For the manual method, no additional guidance was provided in the first group and the technician tried to isolate the screw in the center plane. The second group that was processed manually, the microCT-derived markings on the outside of the resin block served as guidance for the technician. Phantoms in the third group were processed using the novel automated workflow. After the each cut we compared the planned microCT plane with the resulting section and rigidly registered both.The mosaic overlay shows a high degree of alignment, which was quantified using the IoU score. Here matching pixels were colored white, while pixels belonging to the histological section or microCT were assigned either red or green. For the calculation we neglected the green pixels of the plastic screw head since it was not visible in the scan.

H. Automatized guided sectioning facilitates image fusion of microCT and histology

Through the alignment of the 2D histological and the 3D microCT data, the color information was transferred and fused with higher-level features visible in the *in silico* scan. As shown in Figure 8 we performed this multimodal fusion for both a healthy and a rat knee joint with osteolytic lesions. The specimens were intentionally cut at an angle non-parallel to the axes of the CT data set. In Figure 8 a high-quality image registration is demonstrated by the overlaid cone regions. The conic reference structures shown here are based on those used in the comparative study detailed in Part G and serve as an additional marker for the registration process. In the rat knee metastasis example, the bone was destroyed massively by osteolytic lesions that were hindering the alignment of the histological section to the microCT data. Therefore, in such a case the cone-shaped reference objects are of great importance since they allow the precise insertion of the histological plane into the *in silico* volume. After the priming cut with the saw, nearly serial sectioning can be performed using laser microtomy at constant angles. Here the sectioned block is slightly ground before it is glued to a new slide and again placed upon the laser. Using guided sectioning and the cone-shaped reference structures described above, these 2D sections were aligned in the 3D microCT scan as depicted in Figure 9 for a rat knee joint specimen. This denotes a major improvement to the classical cutting-grinding technique, for which the generation of consecutive slides is limited. This is a result of grinding the cut specimen, a standard procedure in classical hard tissue histology, to produce slides of sufficient thickness for microscopy. By applying the described automated workflow, the grinding of the cut resin block is significantly reduced. Thus, the presented method minimizes the offsets between each generated histological section and allows for the reconstruction of an *in silico* 3D histological volume through serial registration and correlative imaging. An exemplary alignment of multiple slides is shown in Figure 9, where the distance between the slides was increased to improve the visibility of each histological slice. In summary, because each cut results in a matching pair of a histological section and a corresponding *in silico* slice in the microCT data set the developed novel automated workflow enables correlative imaging, a key technology in digital pathology applications (further examples can be seen in Supplementary Figure 1).

IV. Discussion

We have designed and successfully implemented a novel automated and computer-aided sectioning workflow, which surpasses the conventional manual cutting-grinding techniques applied to resin-embedded specimens. Our approach demonstrates significant improvements in terms of positioning accuracy, minimizing sectioning times, and reduction in material consumption for the generation of histological slides. Notably, the incorporation of a laser microtome in the process enables the introduction of nearly serial sectioning, thereby facilitating the precise extraction of 3D structures for future analyses. For constant cutting angles, only one priming cut is required, which allows the extraction of adjacent ROIs. Furthermore, through the alignment of several histological slides, the color information can be transferred into the 3D context. Additionally, integrating color data with 3D imaging facilitates the identification of subtle histopathological changes that might be overlooked in two-dimensional analysis alone.

Here we demonstrate in direct comparison with the established sectioning routine for resin-embedded specimens that our automated methodology exhibits notable advantages. We achieved a nearly sevenfold increase in precision, and completed the tasks approximately four times faster, while concurrently losing about half the material. The concept of using microCT to identify hidden sites of interest and to use this information to optimize the sectioning process in histology has already been proposed in multiple studies reaching from the generation of a precise model of the human inner ear [18], *targeted sectioning* of FFPE tissue [19], and guided sectioning using an ultramicrotome for subsequent electron microscopic analysis [4]. This highlights the fact that *targeted sectioning* is of high importance in histological tissue analysis. However, to our knowledge, no automated *targeted sectioning* system for larger ($> 2\ cm$) resin-embedded samples as presented here has been implemented before.

The visualization of the contact zone of implant screws by a sectioning routine represents a common task to facilitate the evaluation of osteointegration. Commonly, the desired slice is produced manually, which complicates the targeting of the screw inside the sample. Furthermore, the generation of adjacent slices is difficult, due to the destructive grinding of the block required. In our exemplary slides produced from the phantoms containing screws, for which we marked no cutting guiding lines on the resin blocks, we found that our technician was not able to correctly isolate the center plane. Therefore, we believe that the inclusion of a microCT scan already significantly enriches the targeting of ROIs. Furthermore, by contextualizing our achieved offset of approximately 150 microns relative to the resolution of our scans (118 µm) and employing the suggested methodology outlined in our prior work [11], we can discern and quantify the relative accuracy of our approach. This comparative analysis positions our work within the broader context, allowing for a comprehensive evaluation relative to our peers. Here we score a relative accuracy of 0.79. Meechan et al. [4], who developed a similar positioning system for ultramicrotomes, calculated a mean offset of 3.1 microns while scanning at a resolution of 1 micron, resulting in a relative accuracy of about 0.32. Based on the resolution of our microCT scan, we achieved similar or better results than our peers. Therefore, our method allows for the accurate targeting of ROIs in relation to the microCT resolution and accommodates the larger size (>2 cm) of the sectioned specimen.

With the example of a rat knee containing osteolytic lesions, we demonstrated, that our method can aid in the isolation of

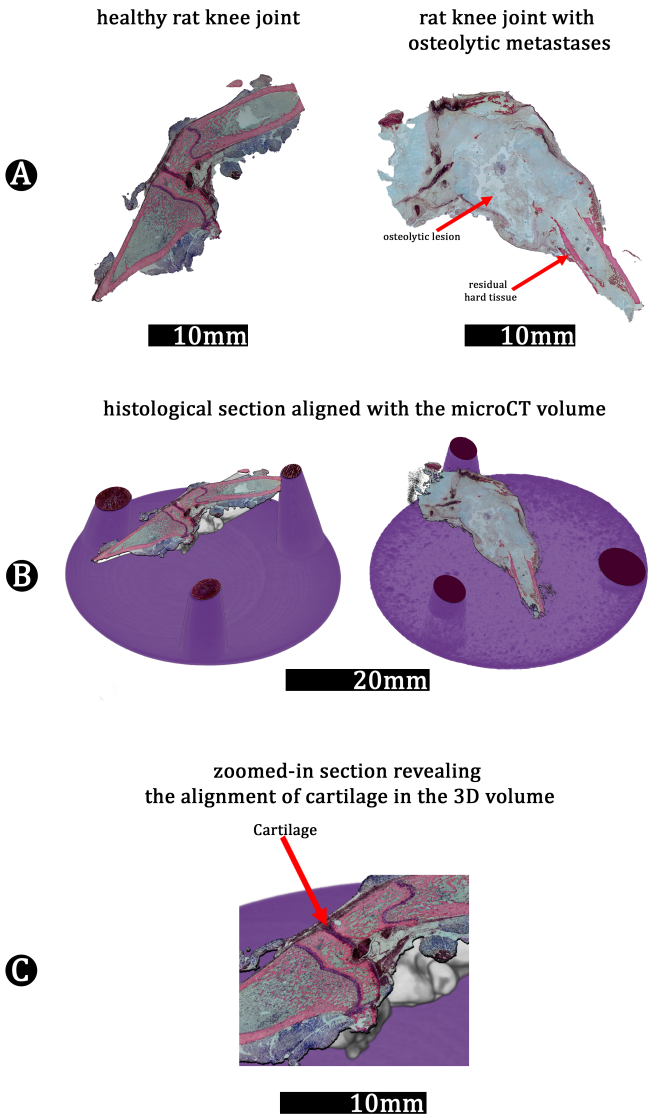

Fig. 8. Multimodal fusion of 2D histological sections produced by the novel workflow and their corresponding 3D microCT volume. The bone sections were stained with a modified Sanderson Rapid Bone Stain [16] followed by a van Gieson [17] counterstaining (A). This resulted in hard tissue staining red to purple, while soft tissue appeared in blue to greenish hues. In order to align these histological sections accurately with the *in silico* volume, cone-shaped reference structures are used, achieving precise registration (B). This alignment allows for the visualization of histological features that are typically not discernible in microCT scans due to insufficient density. For instance, (C) demonstrates the identification of cartilage of a healthy knee joint in the 3D volume, which highlights a significant advantage of this correlative imaging approach by revealing details that are otherwise missed in standard microCT imaging.

the remaining bone tissue and successfully facilitate the fusion of stained histological sections with the *in silico* microCT scan. Based on these preliminary but promising results, we plan to extend the analysis of changes in pathological tissue samples with our correlative imaging approach into the 3D context, thereby enabling the generation of histological sections ideally depicting the interface between healthy and tumor tissue. The alignment of these sections into the 3D context, may aid to improved 3D segmentation of for instance different tumor structures in the future. The nearly serial sectioning, performed with a laser microtome and guided by the established workflow, enables the seamless reconstruction of virtual histological volumes, providing a comprehensive and accurate representation of the tissue's microstructure.

One limiting factor of our approach is the bulkiness of both the resin blocks containing the specimen and the cassette itself. For now, both are placed together within the microCT using a specialized holder, which requires a wider gap between tube and detector. In common microCT systems which use geometrical magnification, such a condition results in severely decreased spatial resolution when increasing the field of view. Another limitation of the cassette is the coverage of an extensive part of the resin block, which then cannot be cut. Thus, we plan to further optimize the cassette to mitigate this problem. Additionally, the accuracy of our

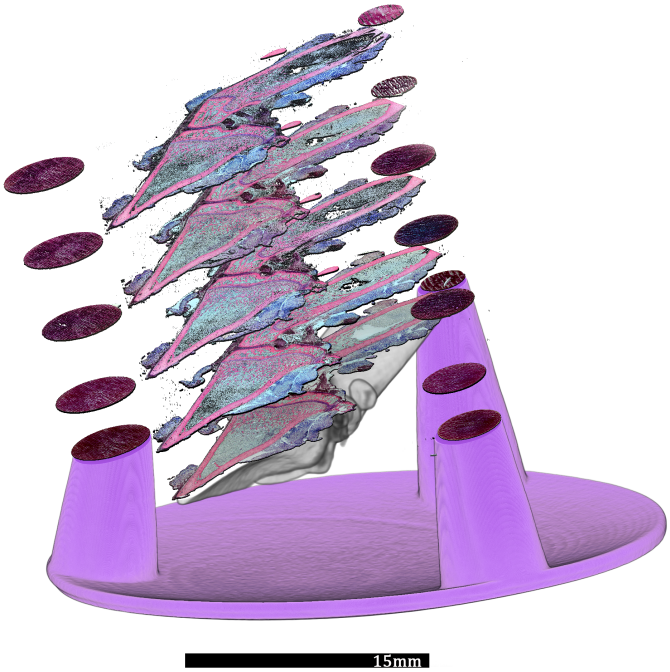

Fig. 9. 3D rendering of microCT scans with 2D histological serial sections, enabling precise alignment and reconstruction of virtual histology volumes. To facilitate clear visualization, the spacing between the histological images was intentionally increased, allowing each section to be easily distinguished. Cone-shaped reference structures were strategically used to verify the position of each slice, ensuring accurate alignment. This alignment was further refined using detailed information obtained during the planning stage of the automated workflow.

approach could be increased by integrating the developed positioning system into a buzz saw-based sectioning machine, instead of the here-used band saw, as we expect significantly less vibration in such a cutting device. In the future, we aim to address the mentioned shortcomings by remodeling our technical setup to be adapted for different saws, allowing for a wider range of applications. Moreover, we hope to reduce the size of our cassette while ensuring equally rigid fixation.

V. Conclusion

In conclusion, the here presented microCT-based *targeted sectioning* workflow for resin-embedded samples successfully reduces the influence of human error by automating the positioning of the block for cutting. This process is further refined using laser microtomy, which allows for the contact-free sectioning of the specimen parallel to the priming cut. This approach minimized the overall material loss and eased the generation of consecutive slices. Due to the demonstrated increased accuracy and higher throughput for the generation of slices, our method can be utilized for the creation of multimodal data sets consisting of 2D histology and 3D microCT imaging data, without the need to manually match each histological slice to a position in a 3D volume, a significant advantage promising to rapidly improve the use and availability of machine learning applications in the field of digital pathology.

VI. Acknowledgments

The authors would thank Ute Kant for sectioning the exemplary slides and the employees of LLS Rowiak for the sectioning of a subset of specimens. Furthermore, the authors thank Leon Grewe and Dipl-Ing. (FH) Reinhard Mollus for the design and crafting of the CT holder for the cassettes and acknowledge the support of Mona Brants who rendered multiple figures presented in this work. Additionally, the authors express their gratitude to Anfisa Eberle for embedding the phantoms used in this study.

VII. Author Contributions

P. Nolte conducted the majority of the software development for the cutting plane planning, positioning, and analysis of the data. He also performed laser microtomy sectioning, and microscopy, contributed to the concept and design process, and drafted this article. C.J. Gröger engineered all mechanical parts in this project. Furthermore, he created the phantoms, contributed to the concept and design process, and ensured high-quality laser microtome sectioning. C. Frey led the mechanical engineering. H. Richter optimized the laser microtomy routine and created some of the sections. F. Will aided in the designing process of the cutting system and helped with the troubleshooting of the laser microtome. T. Bäuerle provided the application case of the rat knee joint. A. F. Schilling improved the analysis pipeline and contributed to the writing process. F. Alves contributed to the experimental design. C. Rußmann led the CT-LASER-BONE project and supervised the hardware development. C. Dullin co-developed the software and led the software design, contributed to the concept, the design process, and the writing process. All authors reviewed, edited, and approved the final article.

VIII. Ethics declarations

This research project adheres to the highest ethical standards, and the principles of integrity and responsibility were rigorously upheld throughout the study. The nature of this investigation involved no human subjects, and no sensitive or confidential information was utilized. The animal experiments were approved by the local animal welfare and ethics committee of Franconia, Germany (55.2 DMS-2532-2-228).

References

[1] K. Donath, “Die Trenn-Dünnschliff-Technik zur Herstellung histologischer Präparate von nicht schneidbaren Geweben und Materialien: Apparate- und methodenbeschreibung”, 1988.

[2] J. Albers et al., “X-ray-based 3d virtual histology—adding the next dimension to histological analysis”, Mol. Imaging Biol., vol. 20, no. 5, pp. 732–741, 2018. [Online]. Available: https://doi.org/10.1007/s11307-018-1246-3

[3] J. Albers et al., “Elastic transformation of histological slices allows precise co-registration with microCT data sets for a refined virtual histology approach”, Sci. Rep., vol. 11, no. 1, p. 10846, 2021. [Online]. Available: https://doi.org/10.1038/s41598-021-89841-

[4] K. Meechan et al., “Crosshair, semi-automated targeting for electron microscopy with a motorised ultramicrotome”, eLife, vol. 11, p. 80899, 2022. [Online]. Available: https://doi.org/10.7554/eLife.80899

[5] Y. Hua, P. Laserstein, and M. Helmstaedter, “Large-volume en-bloc staining for electron microscopy-based connectomics”, Nat. Commun., vol. 6, no. 1, p. 7923, 2015. [Online]. Available: https://doi.org/10.1038/ncomms8923

[6] N. Kawata et al., "Micro-computed tomography: A novel diagnostic technique for the evaluation of gastrointestinal specimens", Endosc. Int. Open.,vol. 9, no. 12, pp. E1886-E1889, 2021, [Online]. Available: https://doi.org/10.1055/a-1546-8063

[7] B. D. Metscher, "MicroCT for comparative morphology: simple staining methods allow high-contrast 3D imaging of diverse non-mineralized animal tissues", BMC Physiol., vol. 9, no. 1, p. 11, 2009. [Online]. Available: https://doi.org/10.1186/14 72-6793-9-11

[8] A. Teplov et al. "Development of Standard Operating Procedure (SOP) of Micro-computed tomography (micro-CT) in Pathology", Diagn. Pathol., vol. 5, no. 1, 2019. [Online]. Available: https://doi.org/10.17629/www .diagnosticpathology.eu-2019-5:273

[9] H. Lubatschowski, "Laser Microtomy", Optik & Photonik, vol. 2, no. 2, pp. 49–51, 2007. [Online]. Available: https://doi.org/10.1002/opph.201190252

[10] C. Kunert-Keil et al., "Histological comparison between laser microtome sections and ground specimens of implant-containing tissues", Ann. Anat., vol. 222, pp. 153–157, 2019. [Online]. Available: https://doi.org/10.1016/j .aanat.2018.12.001

[11] P. Nolte et al., "Current Approaches for Image Fusion of Histological Data with Computed Tomography and Magnetic Resonance Imaging", Radiol. Res. Pract., 2022, p. 6765895, 2022. [Online]. Available: https://doi.org/10.1155/2022/6 765895

[12] P. Nolte et al.,"Spatial correlation of 2D hard-tissue histology with 3D microCT scans through 3D printed phantoms", Sci. Rep., vol. 13, no. 1, p. 18479, 2023. [Online]. Available: https://doi.org/10.1038/s41598-023-45518-0

[13] R. O. Duda and P. E. Hart, "Use of the Hough transformation to detect lines and curves in pictures", Commun. ACM, vol. 15, no. 1, pp. 11–15, 1972.

[14] K. Pearson, "On lines and planes of closest fit to systems of points in space", Lond., Edinb., Dublin Philos. Mag. J. Sci., vol. 2, no. 11, pp. 559–572, 1901. [Online]. Available: https://doi.org/10.1080/14 786440109462720

[15] V. A. Stadelmann et al.,"Longitudinal time-lapse in vivo micro-CT reveals differential patterns of peri-implant bone changes after subclinical bacterial infection in a rat model", Sci. Rep., vol. 10, no. 1, p. 20901, 2020. [Online]. Available: https://doi.org/10.1038/s41598-020-77770-z

[16] C. Sanderson and K. N. Bachus, "Staining technique to differentiate mineralized and demineralized bone in ground sections", J. Histotechnol., vol. 20, no. 2, pp. 119–122, 1997. [Online]. Available: https://doi.org/10.1179/his.1997.20.2.119

[17] F. H. Verhoeff, "Some new staining methods of wide applicability: including a rapid differential stain for elastic tissue", JAMA, vol. L, no. 11, pp. 876–877, 1908. [Online]. Available: https://doi.org/10.1001/jama.1908.25310370042004a

[18] T. S. Rau et al., "Three-dimensional histological specimen preparation for accurate imaging and spatial reconstruction of the middle and inner ear", Int. J. Comput. Assist. Radiol. Surg., vol. 8, pp. 481–509, 2013. [Online]. Available: https://doi.org/10.1007/s11548-013-0825-7

[19] J. Albers et al., "X-ray based virtual histology allows guided sectioning of heavy ion stained murine lungs for histological analysis", Sci. Rep., vol. 8, no. 1, p. 7712, 2018. [Online]. Available: https://doi.org/10.1038/s41598-018-26086-0

[20] T. Bäuerle et al., "Treatment of bone metastasis induced by mda-mb-231 breast cancer cells with an antibody against bone sialoprotein", Int. J. Oncol., vol. 28, no. 3, pp. 573–583, 2006. [Online]. Available: https://doi.org/10.3892/ijo.28.3.573

[21] M. U. Ghani et al., "Investigation of spatial resolution characteristics of an in vivo micro computed tomography system", Nucl. Instrum. Methods Phys. Res. A, vol. 807, pp. 129–136, Jan. 2016. [Online]. Available: https://doi.org/10.1016/j .nima.2015.11.007

[22] W. Schroeder, K. Martin, and B. Lorensen, "The Visualization Toolkit: An Object-Oriented Approach to 3D Graphics", 1998. [Online]. Available: https://vtk.org/vtk-textbook/

[23] G. Bradski, "The OpenCV library", Dr. Dobb's J. Softw. Tools, vol. 25, no. 11, pp. 120–126, 2000.

[24] T. Q. Company, "Qt", [Online; accessed 10 November 2023]. [Online]. Available: https://www.qt.io/

[25] C. R. Harris et al., "Array programming with NumPy", Nature, vol. 585, no. 7825, pp. 357–362, 2020. [Online]. Available: https://doi.org/10.1038/s41586-020-2649-2

[26] F. Pedregosa et al., "Scikit-learn: Machine learning in Python", J. Mach. Learn. Res., vol. 12, pp. 2825–2830, 2011.

[27] S. Walt et al., "scikit-image: image processing in Python", PeerJ, vol. 2, p. 453, 2014. [Online]. Available: https://doi.org/10.7717/peerj.453

[28] R. Beare, B. Lowekamp, and Z. Yaniv, "Image Segmentation, Registration and Characterization in R with SimpleITK", J. Stat. Softw., vol. 86, no. 8, pp. 1–35, 2018. [Online]. Available: https://doi.org/10.18637/jss.v086.i08

[29] T. Kluyver et al., "Jupyter Notebooks – a Publishing Format for Reproducible Computational Workflows", in Positioning and Power in Academic Publishing: Players, Agents and Agendas, F. Loizides and B. Schmidt, Eds. IOS Press, 2016, pp. 87–90.

[30] P. Ramachandran and G. Varoquaux, "Mayavi: 3D Visualization of Scientific Data", Comput. Sci. Eng., vol. 13, no. 2, pp. 40–51, 2011.